Oxidation effects on ultrathin Ni and Cr films grown on Fe(001): A combined scanning tunneling microscopy and Auger electron spectroscopy study

M. Riva *, A. Picone, G. Bussetti, A. Brambilla, A. Calloni, G. Berti, L. Duò, F. Ciccacci, M. Finazzi

CNISM—Dipartimento di Fisica, Politecnico di Milano, Piazza Leonardo da Vinci 32, 20133 Milano, Italy

Article history:
Received 18 June 2013
Accepted 18 October 2013
Available online 7 November 2013

1. Introduction

The growth and characterization of thin epitaxial oxide films on metal supports is attracting considerable scientific interest in the last years [1–6]. Indeed, obtaining well defined and atomically flat oxide surfaces allows the study of the fundamental mechanisms underlying a number of physical and chemical phenomena occurring on complex oxide materials, otherwise difficult or impossible to investigate at the atomic level.

Ultrathin transition metal oxide (TMO) films grown on noble metals are routinely used as a model system for the study of a number of complicated physical and chemical phenomena, such as the chemical reactions involved in heterogeneous catalysis [7,8], water interaction with surfaces [9,10], growth of metal particles or films on oxide surfaces [11–13], to name just a few.

Comparatively much less work has been performed on ultrathin TMO films supported on a magnetic substrate such as Fe. TMO/Fe heterostructures, where the TMO films were anti-ferromagnetic NiO or CoO, have been widely investigated by using spectroscopic techniques (for recent reviews see Refs. [14,15]). These structures, besides being model systems for the exchange bias phenomenon, have proven to be an appealing object of study on its own. Indeed, a rich variety of exotic micromagnetic structures have been reported in the literature, ranging from the stabilization of nano-sized magnetic domains in Fe/NiO/Fe trilayers [16], to the stabilization of anti-ferromagnetic vortex states in CoO/Fe/Ag(001) disks [17].

However, atomic scale investigations of TMO/Fe systems by means of scanning probe techniques are still scarce (see for instance Ref. [18]). Such a lack of completeness in the literature mainly originates from the difficulty in preparing samples characterized by a suitable morphology and by chemically abrupt interfaces. Indeed, due to the high reactivity of Fe toward oxygen, during the oxide growth by means of reactive deposition (i.e. metal deposition in oxygen atmosphere), considerable Fe oxidation occurs [18–20]. This results in the development of rough morphologies and/or not well defined interfaces, which are difficult to investigate at the atomic scale with scanning probe techniques.

Obtaining nano-structured TMO films supported on Fe could produce immense advances in the understanding of such TMO/Fe heterostructures, especially by considering the great progresses recently achieved in the direct observation of spin structures down to the atomic scale by means of spin polarized scanning tunneling microscopy (STM) and spectroscopy (STS) (for recent reviews see Refs. [21,22]). In order to successfully achieve atomic level control of TMO/Fe heterostructures, a detailed knowledge of the basic mechanisms driving the growth of TMO thin films and the formation of the TMO/Fe interfaces is required.

In this frame, we have recently investigated Ni and Cr films deposited on the oxygen saturated Fe(001)-$p(1 \times 1)$O surface as model systems for the TMO/Fe interface [23,24]. In those works we exploited the oxygen adsorbed on the Fe(001)-$p(1 \times 1)$O surface before metal deposition in order to explore the possibility to stabilize a single TMO layer on Fe, avoiding at the same time the Fe oxidation occurring when reactive deposition is employed. We found that, despite the good lattice matching

* Corresponding author.
E-mail address: michele.riva@polimi.it (M. Riva).

between NiO and Fe(001), a single layer of NiO on top of the Fe(001) surface could not be stabilized, the growth being characterized by the formation of two-layer-thick Ni islands [23]. On the other hand, submonolayer Cr deposition on the Fe(001)-$p(1 \times 1)$O surface leads to the stabilization of perfect Cr oxide wetting layers on top of Fe(001) [24].

Motivated by our previous investigations and by the fact that Cr_2O_3 and NiO are both anti-ferromagnetic insulators, in the following we show detailed results about the effects induced by the exposure to a controlled amount of molecular oxygen on ultra-thin (4 ML) and continuous Cr and Ni films. We decided to use post-oxidation as a method of preparation in order to investigate the effect of oxygen dosing on thin metallic films pre-deposited on Fe, avoiding at the same time the direct contact of oxygen with Fe, which typically occurs during the early stages of metal deposition in oxygen atmosphere. The film thickness was chosen to be small enough to allow the investigation of the influence of the Fe substrate during the early stages of oxygen exposure.

The aim of the present work is twofold:

i) understanding the chemical reactions occurring in the early stages of oxidation of ultra-thin metallic films grown on Fe(001);
ii) investigating the morphology of the oxidized films and the effects of annealing treatments on the surface order.

Our findings indicate that, as soon as the oxygen is dosed on ultra-thin Ni films grown on the Fe substrate, Fe atoms segregate toward the surface, where their oxidation takes place. Increasing the oxygen exposure induces the formation of a highly ordered FeO(111)-like overlayer.

On the contrary, in the Cr/Fe(001) system we managed to oxidize the entire film while keeping the Fe substrate in its metallic state. However, the resulting morphology is rough and thermal treatments are not able to improve the order of the surface.

2. Experimental details

Samples were prepared in an ultra-high vacuum (UHV) system (base pressure $< 1 \times 10^{-10}$ mbar) by starting from a UHV-cleaned MgO(001) single crystal substrate, over which a 400 nm thick Fe(001) film was grown by means of molecular beam epitaxy (MBE).

Cr and Ni films 4 ML thick were grown onto Fe(001) substrates by MBE under UHV conditions, with a typical growth rate of about 1 equivalent monolayer[1] (ML) per minute, as measured by a quartz microbalance. The substrate was kept at room temperature (RT) during the Ni and Cr depositions.

Film oxidation was performed by admitting molecular oxygen from a leak valve. The oxygen partial pressure during the oxidation was 10^{-9} mbar for the lowest exposure ($10\ \mathrm{L} = 1.3 \times 10^{-5}$ mbar $\times$ s) and 10^{-7} mbar for the highest one (150 L). Starting from the oxygen-free sample, the oxygen dose was incrementally increased.

After each step of oxidation, before STM and Auger characterization, the samples were annealed at mild temperatures (200 °C) in UHV in order to improve the film morphology. When the maximum oxygen exposure considered in the present paper (150 L) was reached, a final annealing in UHV conditions was performed. In the case of Ni/Fe a single annealing step at 300 °C for 5 min was performed. A different Ni film (approximately 5 ML thick) grown on Fe(001) at RT was moreover incrementally exposed to oxygen following the same dose steps above (from 10 to 150 L). Such a sample was not subject to post-annealing treatments until the highest exposure was reached. A final annealing step at mild temperatures (200 °C) was subsequently carried out. On the other hand, for the Cr/Fe(001) system, several annealing steps were used, up to a maximum temperature of 700 °C.

STM measurements were performed by using an Omicron Variable Temperature STM in a UHV chamber connected to the preparation system. STM images were acquired at room temperature in constant-current mode with home-made electrochemically etched W tips.

The low energy electron diffraction (LEED) and Auger electron spectroscopy (AES) analysis was performed by means of an Omicron SPECTALEED with a retarding field analyzer (total acceptance angle 102°). A 3 kV, 20 μA electron beam was used, with a 3 V peak-to-peak modulation amplitude.

3. Ni/Fe(001) oxidation

3.1. Auger data

In order to investigate the chemical reactions occurring during oxidation we measured low-energy Auger peaks, corresponding to MNN transitions. Indeed, the shape of these peaks has proven to be extremely sensitive to the local chemical environment of the atoms (see for instance Refs. [25–27] for Fe oxides and Refs. [28,29] for Ni oxidation). However, attention must be paid in the interpretation of such low-kinetic-energy features, in particular for what concerns the correlation between their position and the exact oxidation state of the element. For instance, Sault demonstrated that the Fe(MNN) lineshape for Fe_3O_4 and Fe_2O_3 are extremely similar, and cannot be used to discriminate between these two oxides [25]. We can thus safely consider the change in the shape of these peaks as a fingerprint of oxidation, although further pieces of information are required in order to establish which oxide is actually formed.

Fig. 1(a) displays the Auger spectra acquired after each step of oxidation in the low kinetic energy region from the 4 ML thick Ni/Fe(001) film. As a reference, in the top part of Fig. 1 we report the Auger spectra acquired on the Fe(001)-$p(1 \times 1)$O (i.e. on the surface covered by one oxygen monolayer) [30–34] and on the Fe oxide obtained by exposing the pristine Fe(001) (i.e. without Ni) to 50 L of molecular oxygen.

In the spectrum of the as-grown sample, before the oxidation, two main features are visible at 47 eV and 61 eV, characteristic of metallic Fe and Ni, respectively. After 10 L exposure a shoulder appears at lower kinetic energy with respect to the metallic Fe peak. Such a shoulder is analogous to the one present on the Fe(001)-$p(1 \times 1)$O surface, suggesting that, at this stage, Fe is starting to get oxidized. The Ni peak is attenuated not exhibiting any significant chemical shift. Increasing the oxygen exposure up to 60 L clearly enhances the intensity of the peaks associated with Fe oxide, while the feature related to Ni almost disappears. Further increase of the oxygen exposure up to 150 L and the final annealing at 300 °C in UHV do not significantly change neither the shape nor the intensity of the measured peaks.

Fig. 1(b) displays the high kinetic energy region, in which the features due to Ni and Fe LMM transitions are visible. After a 10 L exposure to O_2 the O KLL features appear, without any substantial change in the intensity of Ni and Fe peaks. At higher oxygen dose the Ni peaks are considerably attenuated, although still visible, indicating that some Ni is present underneath the Fe oxide film. Due to the post-annealing treatment it is likely that such Ni is partially intermixed with Fe at the interface.

In Fig. 1(c) the intensity of the oxygen peak as a function of oxygen exposure is reported. After exposure to 10 L the peak-to-peak intensity is comparable to that measured on the Fe(001)-$p(1 \times 1)$O surface, suggesting that the adsorbed oxygen approximately amounts to a single atomic layer. The O signal is almost saturated after exposure to 60 L of oxygen and further dosage causes a variation of only a few percent of the measured intensity.

3.2. Morphology and structure

STM images acquired after each oxidation step are presented in Fig. 2. Fig. 2(a) shows the STM topography of the Ni film before the oxidation. As observed in our previous investigations, Ni grows on the clean Fe(001) surface following an almost perfect layer-by-layer mechanism, with only few pits (covering approximately 5% of the surface and

[1] One equivalent monolayer (1 ML) equals the amount of atoms required to completely saturate the adsorption sites on the Fe substrate, i.e., about 12.2×10^{14} atoms/cm^2.

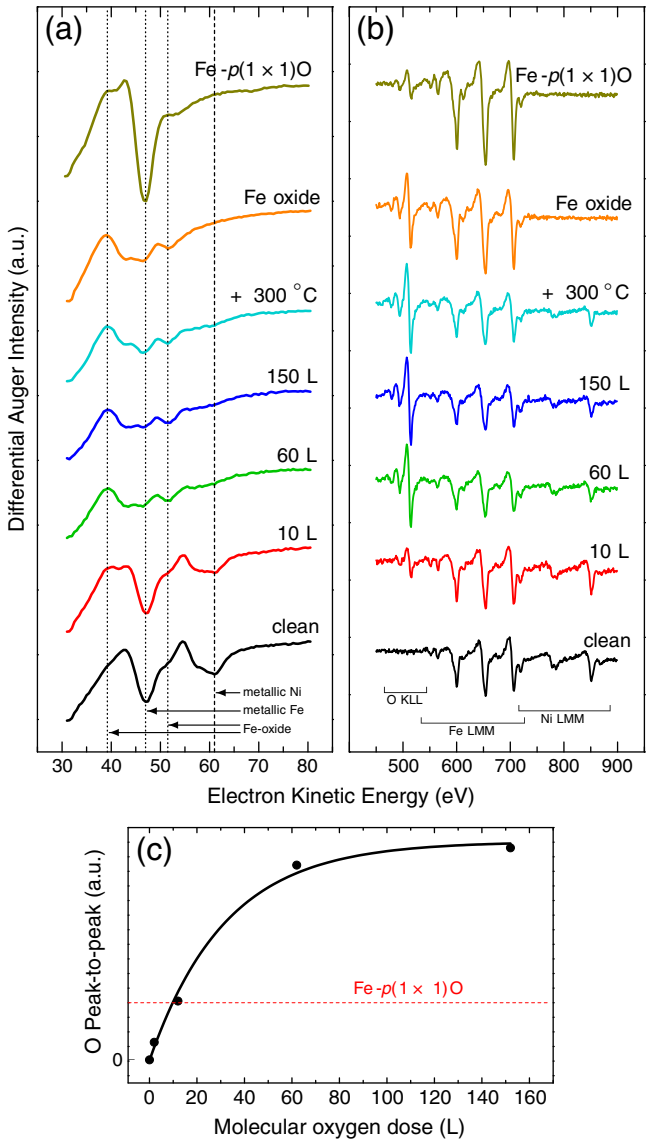

Fig. 1. (a) Fe and Ni MNN AES lineshape as a function of oxygen exposure and annealing temperature. The topmost spectra were acquired for comparison on the Fe(001)-$p(1 \times 1)$O surface and a Fe(001) sample exposed to 50 L of oxygen, respectively. The position for characteristic Fe (dotted) and Ni (dashed) features is indicated. (b) Corresponding Fe LMM, Ni LMM and O KLL transitions. (c) Oxygen KLL peak-to-peak intensity as a function of the dose. The horizontal dashed red line refers to the oxygen signal from the Fe(001)-$p(1 \times 1)$O surface (one oxygen monolayer). (For interpretation of the references to color in this figure legend, the reader is referred to the web version of this article.)

140 pm deep) present on the surface [23,35,36]. We did not manage to obtain atomic resolution on this sample, although in the LEED pattern (not shown) a square symmetry with a $p(1 \times 1)$ periodicity with respect to the Fe lattice was observed, indicating that the Ni film is in its metastable body centered cubic phase.

Exposure to 10 L of oxygen induces a flattening of the surface [see Fig. 2(b)]. Due to the presence of the oxygen overlayer, the atomic corrugation measured in STM images is larger with respect to the clean surface and it is possible to obtain atomically resolved images [see the inset in Fig. 2(b), acquired on the atomic layer covering approximately 90% of the surface], showing a lattice with square symmetry and in-plane spatial periodicity equal to that of the Fe(001)-$p(1 \times 1)$O surface (2.87 Å).

Increasing the oxygen exposure to 60 L induces a roughening of the surface [see Fig. 2(c)]. At this stage the LEED pattern displays faint spots arranged with a quasi-hexagonal symmetry (not shown).

Fig. 2(d) displays the sample morphology after exposure to 150 L of molecular oxygen and subsequent annealing at 300 °C in UHV conditions. The sample is characterized by large flat terraces, and atomically resolved images show that the unit cell is hexagonal [inset of Fig. 2(d)].

Such a hexagonal arrangement of surface atoms is also detected from the LEED pattern, in which two domains are visible, one 90°-rotated with respect to the other [see Fig. 3(a)]. In order to evaluate the spatial periodicity and the angle between the unit vectors we have analyzed the reciprocal lattice vectors inferred from the LEED pattern. This analysis supplies a real-space slightly distorted hexagonal unit mesh with basis vectors (3.06 ± 0.07) Å and (3.22 ± 0.11) Å long, and an angle of $(61.5 \pm 0.1)°$, as displayed in Fig. 3(b).[2] Considering that the nearest-neighbor spacing between atoms in the FeO(111) surface is $a_{FeO} = 3.04$ Å [37], we can infer that the overlayer consists of a FeO(111) film, which might be characterized by a slightly distorted hexagonal unit cell.

A closer inspection of the LEED pattern reveals that the diffraction spots are elongated and split along mutually perpendicular directions [see inset in Fig. 3(a)]. These LEED features are related to the periodic buckling visible in the STM images. In particular we observe a buckling with a largely variable periodicity ranging from about 7 to 15 nm [Figs. 2(d), 4(a) and (b)] and another one with a shorter period of 2.36 nm [see Fig. 4(c) and (d)], mutually orthogonal in a given domain. The latter is confirmed by the analysis of the LEED spot splitting [Fig. 3(a) and (b)] which gives a (2.24 ± 0.22) nm periodicity along the $\mathbf{a}_1$ direction. In order to understand the origin of these two mesoscopic-range periodic modulations, we have tried to superimpose the surface hexagonal lattice with a square lattice with the same in-plane spatial periodicity of the Fe(001) substrate, aligning the $\mathbf{a}_1$ vector with one of the Fe(001) main crystallographic axes as suggested by the LEED pattern. Fig. 4(e) shows the result of such a superposition, from which it is possible to notice that the height modulation is due to an interference between the quasi-hexagonal top-layer and the subsurface bcc-(001) layer, resulting in a quasi-coincidence superlattice. The long-period modulation [Fig. 4(b)] can be attributed to quasi-coincidence along the direction perpendicular to the $\mathbf{a}_1$ unit vector.

3.3. Oxygen versus temperature influence

In order to discriminate among the influence of oxygen exposure and post-annealing on the Fe segregation, a different 5 ML thick Ni/Fe(001) film was incrementally exposed to oxygen avoiding any post-annealing treatment up to the highest dose.

Fig. 5(a) reports the Auger spectra acquired after each step of oxidation in the low kinetic energy region for the 5 ML thick Ni/Fe(001) film. Spectra were acquired at normal emission (solid curves) as well as tilting (77°) the sample normal with respect to the incident electron beam (dashed curves). The topmost spectra in Fig. 5(a) refer to the final mild-annealed sample.

In the spectra of the as-grown sample the two characteristic features of metallic Fe and Ni are clearly visible, the former being notably attenuated while the latter being substantially unaffected upon tilting the sample, respectively. Such an observation suggests that significant Fe segregation on top of the Ni film can be excluded in this case. This is in nice agreement with the lower surface energy of metallic bcc Ni (2.000 J/m^2 [38]) as compared with Fe (2.222 J/m^2 [39]), which should result in stable Ni films on Fe(001). However, generally speaking, we cannot rule out the chance that a small amount of Fe atoms are intermixed in the Ni film. On the other hand Mijiritskii et al. [40] did not detect by X-ray photoelectron spectroscopy any intermixing while depositing Ni

[2] The unit vector lengths are derived comparing spot–spot distances on the LEED patterns from the sample and the pristine Fe(001) surface at the same electron energy. Similar results are obtained for the LEED pattern measured at 100, 150 and 200 eV. Uncertainties on the basis vectors length and relative orientation are derived from the Gaussian shape of LEED spots.

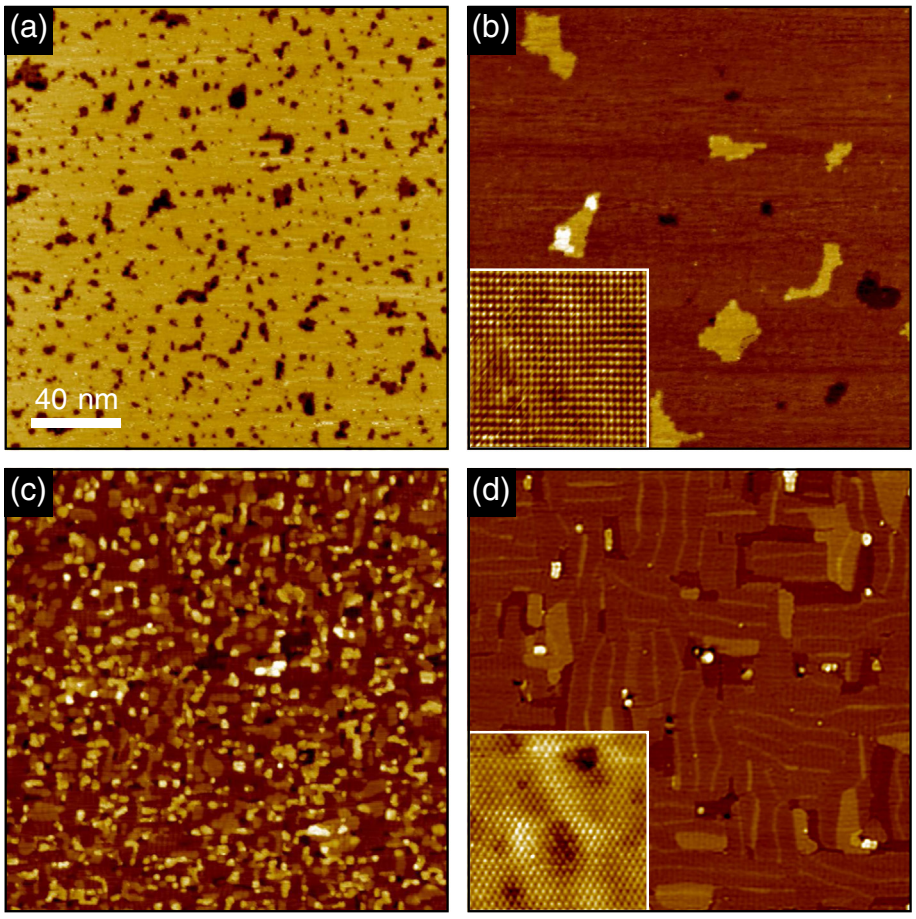

Fig. 2. STM morphology ($I_t = 1$ nA, $V_{bias} = 1$ V) for the Ni/Fe(001) sample after oxygen exposure and post-annealing treatments. (a) Pristine Ni/Fe(001); (b) after 10 and (c) after 150 L exposure to O_2; (d) 150 L exposure to O_2 + 5 min annealing at 300 °C. Atomically resolved images (7.5 × 7.5 nm^2, $I_t = 5$ nA, $V_{bias} = 0.1$ V) are reported in the inset of (b) and (d). (For interpretation of the references to color in this figure legend, the reader is referred to the web version of this article.)

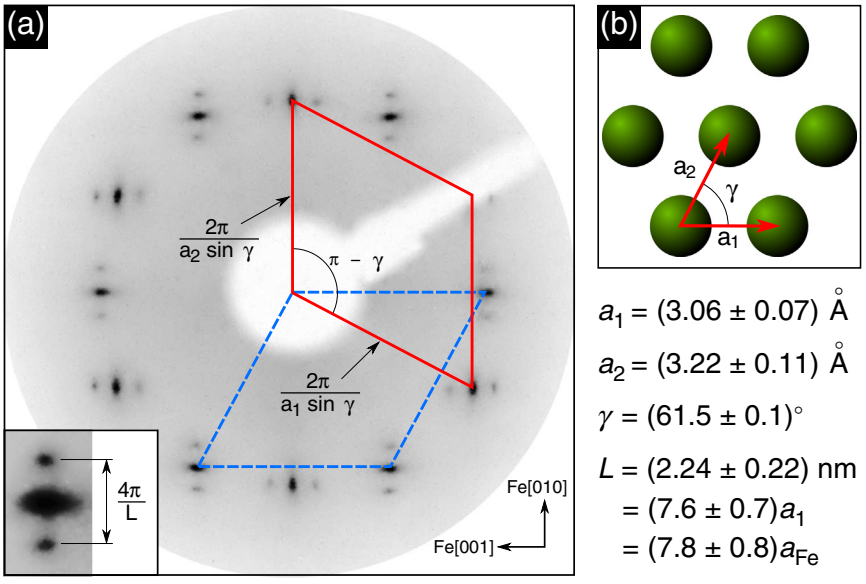

Fig. 3. (a) LEED pattern (100 eV primary energy) of the Ni/Fe sample after exposure to 150 L of oxygen and annealing at 300 °C. Two rotational quasi-hexagonal domains are visible whose reciprocal unit cells are reported in red (solid line) and blue (dashed line). The substrate's main crystallographic directions are indicated. A magnified view of one of the spots is reported in the inset, where the contrast has been purposely increased to enhance the visibility of the mutually orthogonal elongation and spot splitting. The relevant parameters measured from the pattern to obtain the real-space atomic unit cell (main panel) and the supercell periodicity (inset) are indicated. (b) Model of the real space atomic Bravais lattice for the quasi-hexagonal overlayer as obtained from the LEED pattern in (a). The numerical values of the parameters are also reported. (For interpretation of the references to color in this figure legend, the reader is referred to the web version of this article.)

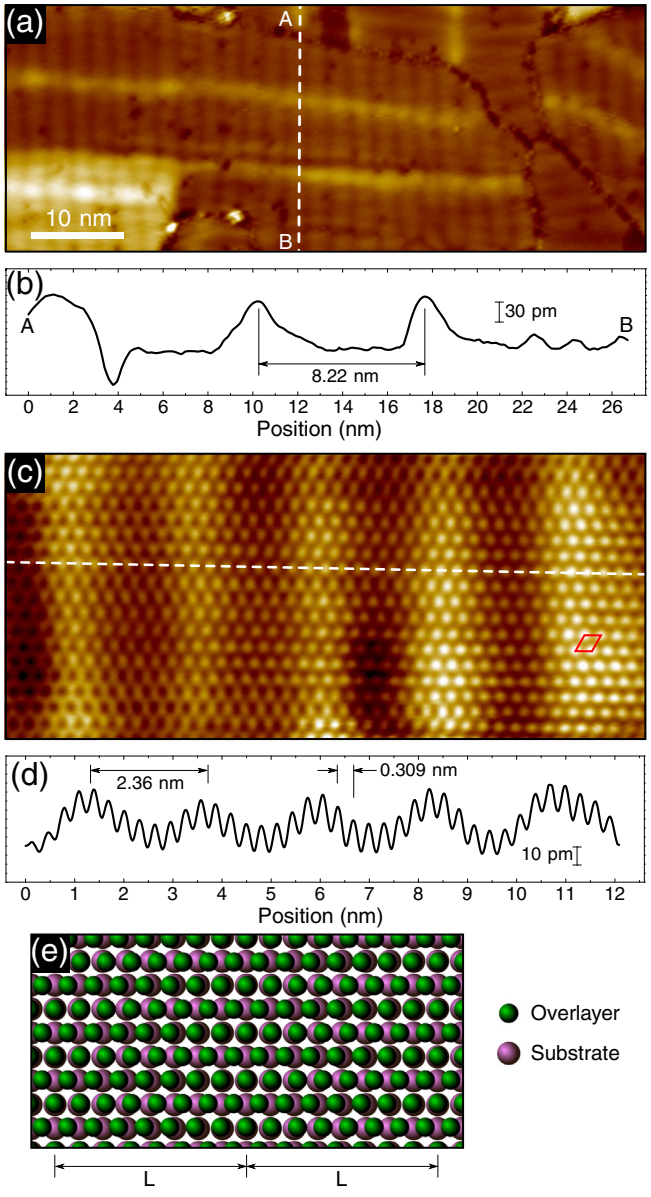

Fig. 4. Ni/Fe exposed to 150 L of oxygen and annealed at 300 °C. (a) Large scale STM topography ($I_t = 1$ nA, $V_{bias} = 1$ V) of several rotational domains showing the mutually orthogonal modulations. (b) Height profile along the dashed white line in (a). The peak-to-peak distance between the maxima of the longer modulation visible in (a) is indicated. (c) Atomically resolved STM topography ($I_t = 5$ nA, $V_{bias} = 0.1$ V) of one of the rotational domains, showing the detail of the short-period modulation. The distorted hexagonal atomic unit cell is indicated in red on the right. (d) Height profile along the dashed white line in (c). The modulation periodicity (L) and the $\mathbf{a}_1$-unit vector length are indicated (refer to Fig. 3 for the notation). (e) Result of the superposition of the distorted hexagonal lattice (green; unit vectors and relative orientation as measured from the LEED pattern in Fig. 3) and a square lattice (violet) with the same spatial periodicity of Fe(001). The short-period modulation results from the quasi-coincidence of the two lattices along the $\mathbf{a}_1$ direction. (For interpretation of the references to color in this figure legend, the reader is referred to the web version of this article.)

on Fe(001) at either RT or even at 150 °C. Considering that Ni was deposited on Fe(001) at RT in our case, we can safely assume that the number of Fe atoms intermixed in the Ni film is negligible.

Upon incrementally exposing the sample to oxygen the evolution of the Auger features is similar to what was observed for the post-annealed sample described in Section 3.1. The metallic Ni and Fe peaks are progressively reduced in intensity, the latter almost vanishing at 60 L total exposure. Moreover, as soon as O is dosed on the film the Fe-oxide feature appears as a shoulder on the low-kinetic energy side of the metallic Fe peak, progressively increasing in intensity with O exposure up to 150 L.

By comparing grazing and normal emission spectra for the oxygen-exposed samples clear and common features can be identified. When the sample is tilted both metallic Ni and Fe peaks are attenuated, while the Fe oxide component is enhanced in each case.

Our results indicate that while O is dosed at room temperature Fe oxidation takes place in the near surface region while metallic Ni remains confined in the subsurface layers. On the other hand, these data do not preclude the possibility that, during exposure to oxygen, a fraction of the Ni atoms is actually oxidized, thus contributing to the reduction of the intensity of the metallic Ni-related feature.

A mild temperature anneal of the sample [topmost spectra in Fig. 5(a)] results in a substantial decrease of the intensity of the metallic Ni peak and an enhancement of the Fe-oxide feature. Once again, upon tilting the sample, these are further attenuated and increased, respectively. These results indicate that, as a consequence of the mild annealing, a larger number of Fe – O bonds is formed in the proximity of the sample surface as compared to the oxygen-exposed film, metallic Ni still lying in subsurface sites. Considering the intermixing tendency of Ni and Fe, it is, however, likely that an alloyed Ni–Fe phase is formed underneath the oxidized region as a consequence of the annealing treatment. Furthermore, these results do not allow the determination of whether some oxidized Ni atoms are present at the sample surface. On the other hand the higher Gibbs free energy gain [41] in the formation of FeO (−58 kJ/mol) as compared to NiO (−50.6 kJ/mol) suggests that, whenever the kinetic barriers can be overcome, a predominance of FeO is likely to be formed. In this frame the post-annealing treatment should favor the formation of Fe – O rather than Ni – O bonds.

STM images of the sample for a selection of the steps described above are reported in Fig. 5(b–d). The morphology of the as-grown sample [Fig. 5(d)] is slightly rougher as compared to that of the 4 ML Ni/Fe(001) described in Section 3.2, mainly exposing three Ni atomic layers. When O is dosed at RT, 1–5 nm diameter clusters are formed on the surface, resulting in a progressively rougher morphology with increasing O exposure [Fig. 5(c)]. Finally, post-annealing at mild temperatures [Fig. 5(b)] leads to an improvement of the surface morphology which nicely resembles the 4 ML-thick Ni/Fe film [cf. Fig. 2(c)]. Namely the large majority of the sample is covered in FeO(111)-like domains with the characteristic short-range modulation, although a higher number of smaller grains per unit surface is obtained with the present procedure.

In summary, the Auger and STM data suggest that exposing to oxygen continuous ultrathin Ni films on Fe(001) causes the formation of oxidized Fe at the surface. Since a negligible amount of Fe is believed to be intermixed within the as-grown Ni films [40] we suggest that the formation of such an oxide proceeds by migration of Fe atoms toward the sample surface. The post-annealing treatment is found to enhance the formation of such an oxide, resulting in the stabilization of an atomically-ordered Fe oxide film with a final morphology characterized by large atomically-flat domains with a hexagonal atomic structure. Our LEED and STM data strongly suggest that this Fe oxide overlayer is associated with a FeO(111)-like film, below which Ni is still present. We cannot exclude that, as a consequence of the post-annealing treatments at 200 °C an alloyed Ni–Fe phase is formed in proximity of the interface underneath the oxidized layer.

4. Cr/Fe(001) oxidation

4.1. Auger data

Before presenting our results on the oxidation of Cr ultra-thin films deposited on Fe it is useful to summarize the results obtained by Ekelund et al. in the oxidation of (110) and (100) chromium surfaces [42]. According to their investigations, two different spectroscopic features

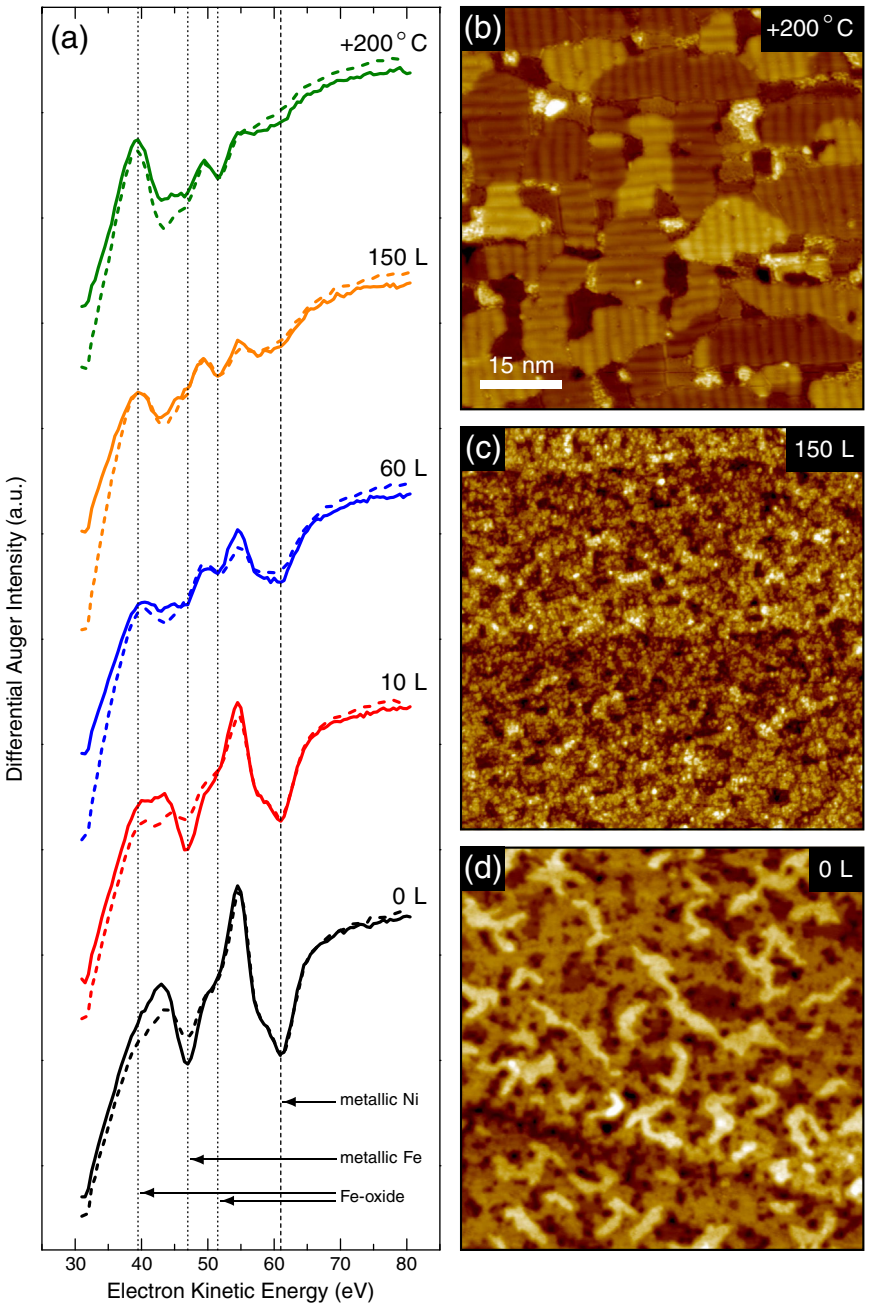

Fig. 5. (a) Low-kinetic energy Auger spectra for the 5 ML-thick Ni/Fe(001) sample at different oxygen exposures. No post-annealing treatment was performed until the highest dose was reached. The topmost spectrum refers to the final sample (150 L oxygen) after a mild-temperature annealing. Solid and dashed curves refer to spectra acquired at normal and grazing (sample normal 77° tilted with respect to the incident electron beam) emissions, respectively. The position of relevant Ni (dashed) and Fe (dotted) transitions is marked by vertical lines. (b–d) STM images ($I_t = 1$ nA, $V_{bias} = 1$ V) for the sample at a selection of the preparation steps. Namely (d) pristine Ni/Fe(001), (c) 150 L and (b) 150 L + 200 °C. (For interpretation of the references to color in this figure legend, the reader is referred to the web version of this article.)

in the low energy Auger spectra are associated to Cr oxidation. The first one, at 31 eV, reaches its maximum amplitude after 10 L of molecular oxygen exposure, being reduced in intensity upon further oxygen dosage. The second one, at 46 eV, increases monotonically in intensity up to 100 L, reaching then a saturation. In our case we can safely use only the peak at 31 eV as a fingerprint of Cr oxidation, since the position of the second feature is extremely close to the position of the signal coming from the metallic Fe substrate (47 eV).

Fig. 6 displays the Auger spectra acquired on the 4 ML Cr/Fe(001) film at increasing oxygen exposures. On the oxygen-free sample the peaks arising from metallic Fe (47 eV) and metallic Cr (36 eV) are visible in the low kinetic energy region [Fig. 6(a)].

After 10 L oxygen dosage the metallic Cr feature is not present anymore, substituted by a peak at 31 eV, related to the formation of Cr oxide. No features related to Fe oxide are visible at this stage while the metallic Fe signal is reduced and presumably superimposed on the Cr oxide 46-eV peak. After 60 L exposure the presence of the spectroscopic features related to Fe oxide is apparent, while the Cr oxide peak at 31 eV is weakened, in agreement with the findings of Ekelund [42]. At such an oxidation stage the metallic-Fe peak has completely disappeared and only the 46-eV Cr-oxide peak is visible. Such a trend is confirmed by the spectra acquired after 150 L exposure, where the Fe oxide peaks become more pronounced and the intensity of the Cr oxide peak at 31 eV further decreases.

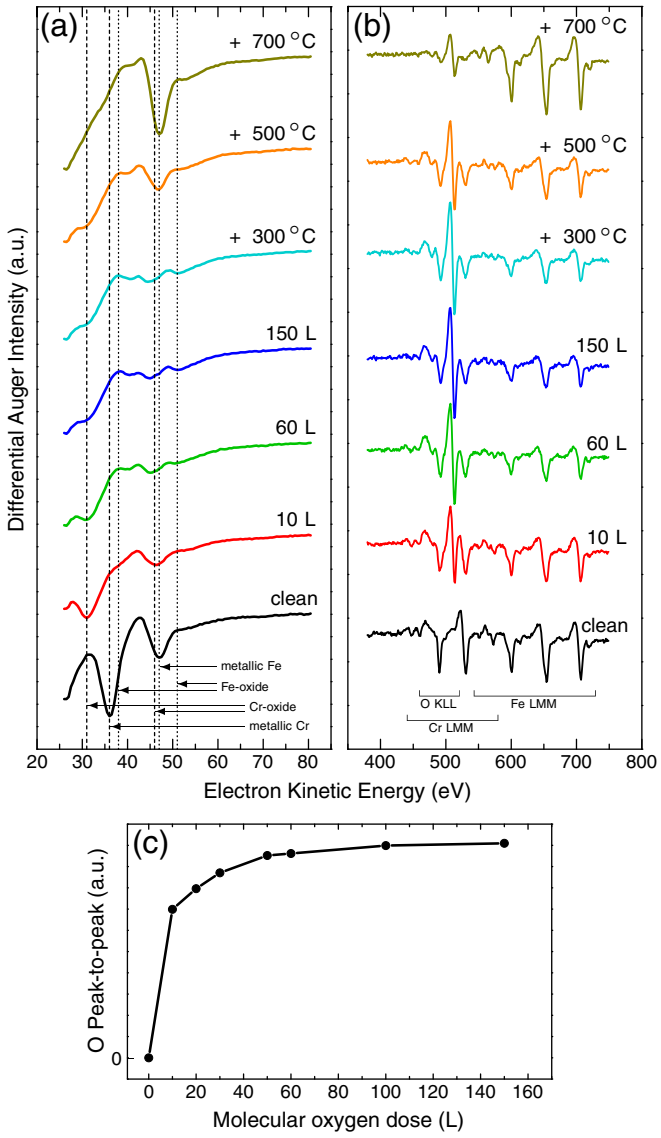

Fig. 6. (a) Low-kinetic energy Auger spectra for the Cr/Fe(001) sample at different oxygen exposures and after post-annealing treatments. The position of relevant features for both Fe (dotted) and Cr (dashed) is indicated. (b) Corresponding high-kinetic energy AES results for the samples in (a). The range of Fe and Cr LMM and O KLL transitions is highlighted. (c) Oxygen peak-to-peak intensity as a function of the dose.

Thermal annealing in UHV conditions at 300 °C does not considerably affect the spectrum. On the other hand, after annealing at 500 °C for 5 min in UHV, the spectrum changes significantly, exhibiting a pronounced rise of the intensity of the peak at 47 eV. Further 5-minute-long annealing steps at 600 °C (not shown) and 700 °C result in a monotonic increase of the Fe-47 eV peak together with a reduction of the Cr and Fe-oxide features, eventually resulting in a spectrum closely resembling that of the Fe(001)-$p(1 \times 1)$O surface [see Fig. 1(a)]. Combining such observations with STM data (see below) we can assume that annealing at 500 °C or above causes a dewetting of the Cr oxide film from the substrate.

Such a conclusion is coherent with the Auger data in the high kinetic energy region where the Fe and Cr LMM and O KLL transitions are visible [Fig. 6(b)]. In fact, after annealing at 500 °C and above, the O and Cr peaks are significantly reduced, while the Fe features increase in intensity, suggesting that the Cr oxide layer is dissolved, resulting in oxygen desorption and Cr atom diffusion into the Fe substrate.

Fig. 6(c) reports the O peak intensity measured as a function of the oxygen dose, from which it is possible to notice that the signal corresponding to oxygen uptake for the Cr/Fe(001) bi-layer is steeper than for the Ni/Fe(001) sample [Fig. 1(c)].

4.2. Morphology and structure

Fig. 7(a) shows the STM topography acquired on the Cr film before the oxidation. Cr grows on the clean Fe(001) surface in a three dimensional mode as apparent from the corresponding line scan, which shows that four layers are exposed [43,44].

After the oxidation step [see Fig. 7(b) and (c) for 10 L and 150 L of oxygen exposure, respectively] the surface is characterized by a rough morphology, preventing the acquisition of atomically resolved images. For this reason we tried to improve the morphology of the film by annealing the sample at increasing temperatures.

Up to 400 °C, these annealing treatments did not significantly affect the sample morphology. In Fig. 7(d) the STM topography obtained after annealing in UHV at 500 °C is reported, showing that some holes are formed in the Cr oxide film. From the STS data [see Fig. 7(e)] it is possible to recognize that on the remaining film a conductivity gap is present. On the contrary, the electronic structure of the holes is different, and strongly resembles the one characteristic of the Fe(001)-$p(1 \times 1)$O, with features at −0.5 eV and +0.9 eV with respect to the Fermi level [34].

Increasing the annealing temperature caused an increase of the surface roughness [see Fig. 7(f)] with a progressively more pronounced dissolution of the Cr oxide film.

These results suggest that annealing the sample above 500 °C causes a dewetting of the Cr oxide from the Fe substrate.

In summary, combining STM and Auger electron spectroscopy data we can conclude that, in the first stages of oxidation (up to 10 L) only the Cr film is oxidized, without any detectable oxidation of the Fe(001) substrate. This film is characterized by a rough morphology. Once the Cr film is completely oxidized, Fe oxidation starts. From our data, however, we can neither discriminate whether the Fe oxidation takes place at the sample surface or at the Cr-oxide/Fe interface, nor establish which kind of Cr oxide is formed. Thermal treatments do not change the composition and morphology of the surface up to 500 °C. Annealing the sample above 500 °C causes a dewetting of the Cr oxide film from the Fe substrate, resulting in a progressive dissolution of the Cr oxide layer with oxygen desorption and Cr diffusion into the substrate.

5. Discussion

The results herein reported indicate that the chemical reactions occurring during the first stages of oxidation of Ni and Cr films grown on Fe(001) are remarkably different. In the case of the Ni film, Fe atoms migrate to the surface, where their oxidation takes place. On the other hand, exposing the Cr film to oxygen leads to a different reaction path, according to which only Cr atoms are initially oxidized.

In a very simple picture, the different chemical behavior observed in the oxidation of Cr and Ni films deposited on Fe could be related to the different oxygen affinity of these two metals with respect to Fe. In this frame, the proximity of the Fe substrate can result in a competition between the substrate's and overlayer's atoms during the early stages of the oxidation process, which favors the oxidation of the metal with the higher oxygen affinity.

In this regard, however, it is worthwhile mentioning the work by Valeri et al. on the oxidation of metastable bct Co (more noble than Fe) films grown on Fe [45,46]. They reported that room temperature oxidation of a 10 ML Co film grown on Fe resulted in a 7 ML thick CoO layer, while at 200 °C the entire film could be oxidized. In both cases no Fe oxidation was reported by the authors.

Another point that deserves some discussion is the observation of the FeO(111)-like film, in view of the fact that rock-salt monoxide surfaces oriented in (111) direction are polar, i.e. a dipole moment

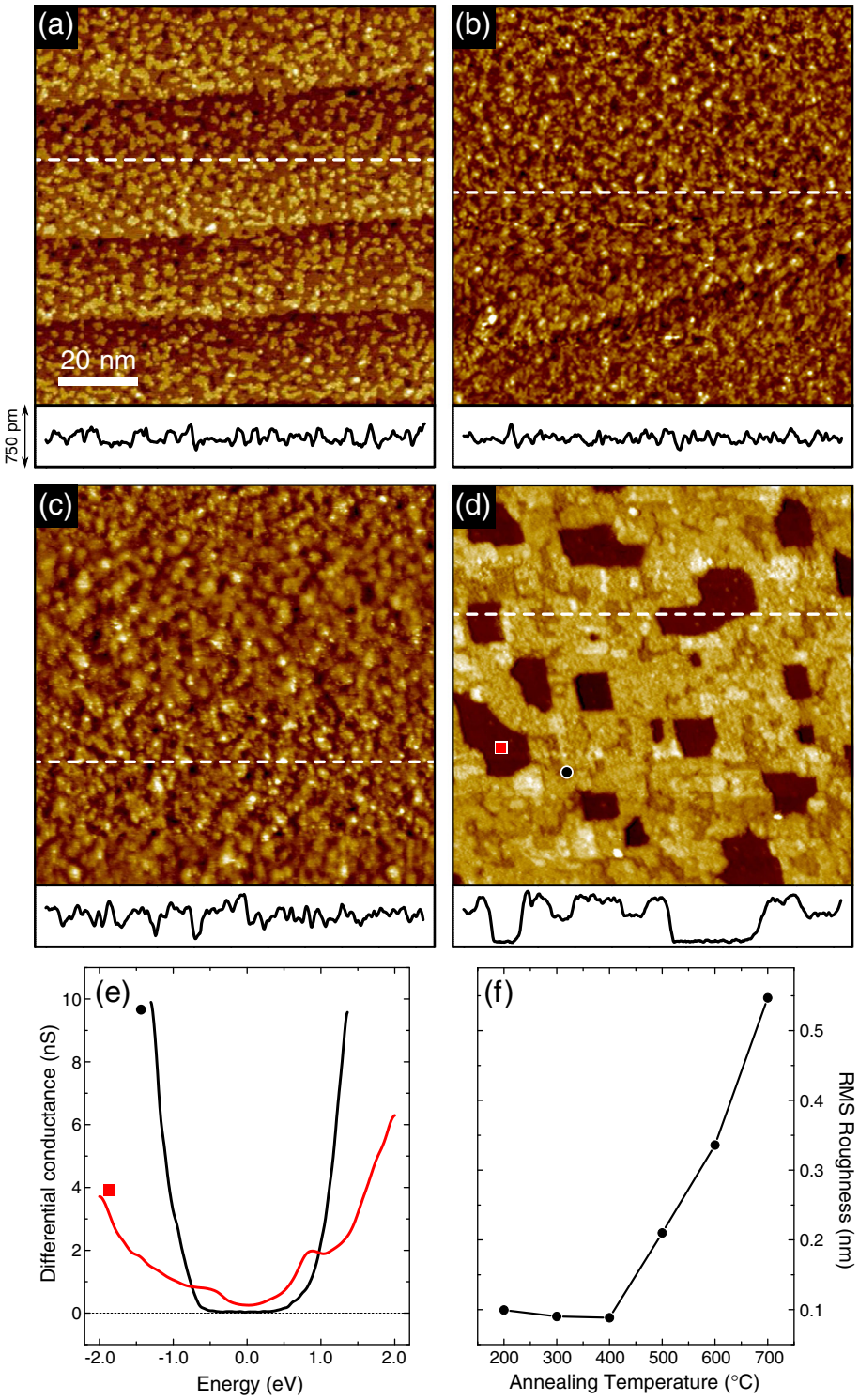

Fig. 7. (a–d) STM topography ($I_t = 1$ nA, $V_{bias} = 1$ V) for the Cr/Fe(001) sample after the oxidation and annealing steps described in the text. (a) Pristine film, (b) 10 and (c) 150 L oxygen exposure, (d) 150 L + 500 °C. Height profiles along the corresponding dashed white lines are reported at the bottom of each panel. Vertical scale is 750 pm. (e) STS spectra ($I_t = 1$ nA, $V_{bias} = 1$ V, lock-in modulation voltage $V_{mod} = 20$ mV RMS) acquired at the corresponding red square and black circle points in (d). (f) Root mean square (RMS) roughness of the sample measured on 200 × 200 nm^2 STM images as a function of the post-annealing temperature. (For interpretation of the references to color in this figure legend, the reader is referred to the web version of this article.)

perpendicular to the surface is present. Bulk-terminated polar surfaces are not stable since alternating layers of oppositely charged ions result in a diverging electrostatic potential [47,48].

However, as long as ultrathin films are considered, the electrostatic potential is finite, and there are several examples in the recent literature showing the possibility to stabilize ultrathin polar films (for the case of FeO(111) see, for instance, Ref. [49]). In order to roughly estimate the thickness of such a film we notice that the oxygen Auger peak-to-peak intensity [Fig. 1(b) and (c)] is approximately 3 times larger than the corresponding intensity measured on the Fe(001)-$p(1 \times 1)$O (in which the oxygen coverage is 1 ML). This evaluation allows us to establish that the final oxide film is composed by at least 3 layers

of oxygen arranged on a close-packed hexagonal lattice, with intercalating hexagonal Fe layers.

In order to discuss the rough morphology observed in the case of Cr oxidation we recall that the most stable Cr oxide is Cr_2O_3, which crystallizes in the corundum structure. Cr_2O_3 films with a (0001) orientation, characterized by an hexagonal lattice symmetry, have been successfully stabilized on hexagonal substrates such as Pt(111) [50] or Ag(111) [51], and on rectangular or centered rectangular substrates such as Cu(011) or Cr(011) [52,53].

Despite the fact that examples of hexagonal epitaxial oxides grown on substrates with a square unit mesh [54] can be found in the literature, in our case the square symmetry of the Fe(001) seems to prevent the growth of epitaxial Cr oxide. In this respect, Fe(011) surfaces could be a candidate for the growth of atomically flat Cr-oxide films on a ferromagnetic substrate.

6. Summary and conclusions

In summary, by combining STM, LEED, and AES we have investigated the early stages of oxidation of ultra-thin Ni and Cr films grown on Fe(001). Our results indicate a quite different behavior of these two systems.

In the case of the Ni/Fe(001) system, since the first stages of oxidation Fe atoms segregate toward the surface, where their oxidation takes place. Thermal treatments performed on the oxidized sample are found to further promote Fe oxidation, leading to the stabilization of a FeO(111)-like overlayer, underneath which Ni atoms are still present, probably alloyed with Fe.

On the contrary, at low oxygen exposures only the Cr film is oxidized, forming a rough oxide that covers the Fe substrate. Upon increasing oxygen exposure Fe oxidation takes place. Thermal annealing of this system does not result in the ordering of the surface and above 500 °C the oxide starts to decompose.

Acknowledgements

This work was partially supported by the Italian Ministry of University and Research through the FIRB project RBAP115AYN.

References

[1] S. Valeri, G. Pacchioni (Eds.), Oxide Ultrathin Films, Wiley-VCH Verlag GmbH & Co. KGaA, 2012, http://dx.doi.org/10.1002/9783527640171.ch1.
[2] S. Surnev, A. Fortunelli, F.P. Netzer, Chem. Rev. 113 (2013) 4314.
[3] F.P. Netzer, Surf. Sci. 604 (2010) 485.
[4] G. Pacchioni, Chem. Eur. J. 18 (2012) 10144.
[5] N. Nilius, Surf. Sci. Rep. 64 (2009) 595.
[6] S.A. Chambers, Surf. Sci. Rep. 39 (2000) 105.
[7] H.-J. Freund, G. Pacchioni, Chem. Soc. Rev. 37 (2008) 2224.
[8] Y.-N. Sun, Z.-H. Qin, M. Lewandowski, E. Carrasco, M. Sterrer, S. Shaikhutdinov, H.-J. Freund, J. Catal. 266 (2009) 359.
[9] L.R. Merte, G. Peng, R. Bechstein, F. Rieboldt, C.A. Farberow, L.C. Grabow, W. Kudernatsch, S. Wendt, E. Lægsgaard, M. Mavrikakis, F. Besenbacher, Science 336 (2012) 889.
[10] W. Wang, H. Zhang, W. Wang, A. Zhao, B. Wang, J. Hou, Chem. Phys. Lett. 500 (2010) 76.
[11] C.T. Campbell, Surf. Sci. Rep. 27 (1997) 1.
[12] N. Nilius, E.D.L. Rienks, H.-P. Rust, H.-J. Freund, Phys. Rev. Lett. 95 (2005) 066101.
[13] P. Luches, F. Pagliuca, S. Valeri, F. Illas, G. Preda, G. Pacchioni, J. Phys. Chem. C 116 (2012) 1122.
[14] M. Finazzi, L. Duò, F. Ciccacci, Surf. Sci. Rep. 64 (2009) 139.
[15] M. Finazzi, L. Duò, F. Ciccacci (Eds.), Magnetic Properties of Antiferromagnetic Oxide Materials: Surfaces, Interfaces and Thin Films, Wiley-VCH Verlag GmbH & Co. KGaA, 2010, http://dx.doi.org/10.1002/9783527630370.
[16] N. Rougemaille, M. Portalupi, A. Brambilla, P. Biagioni, A. Lanzara, M. Finazzi, A.K. Schmid, L. Duò, Phys. Rev. B 76 (2007) 214425.
[17] J. Wu, D. Carlton, J.S. Park, Y. Meng, E. Arenholz, A. Doran, A.T. Young, A. Scholl, C. Hwang, H.W. Zhao, J. Bokor, Z.Q. Qiu, Nat. Phys. 7 (2011) 303.
[18] A. Brambilla, A. Picone, M. Finazzi, L. Duò, F. Ciccacci, Surf. Sci. 605 (2011) 95.
[19] M. Finazzi, A. Brambilla, L. Duò, G. Ghiringhelli, M. Portalupi, F. Ciccacci, M. Zacchigna, M. Zangrando, Phys. Rev. B 70 (2004) 235420.
[20] L. Duò, M. Portalupi, M. Marcon, R. Bertacco, F. Ciccacci, Surf. Sci. 518 (2002) 234.
[21] M. Bode, Chimia 66 (2012) 56.
[22] R. Wiesendanger, Rev. Mod. Phys. 81 (2009) 1495.
[23] A. Picone, G. Bussetti, M. Riva, A. Calloni, A. Brambilla, L. Duò, F. Ciccacci, M. Finazzi, Phys. Rev. B 86 (2012) 075465.
[24] A. Picone, G. Fratesi, M. Riva, G. Bussetti, A. Calloni, A. Brambilla, M.I. Trioni, L. Duò, F. Ciccacci, M. Finazzi, Phys. Rev. B 87 (2013) 085403.
[25] A.G. Sault, Appl. Surf. Sci. 74 (1994) 249.
[26] M. Seo, J. Lumsden, R. Staehle, Surf. Sci. 50 (1975) 541.
[27] G.W. Simmons, D.J. Dwyer, Surf. Sci. 48 (1975) 373.
[28] C. Benndorf, B. Egert, C. Nöbl, H. Seidel, F. Thieme, Surf. Sci. 92 (1980) 636.
[29] P.H. Holloway, J.B. Hudson, J. Vac. Sci. Technol. 12 (1975) 647.
[30] A. Tange, C.L. Gao, B.Y. Yavorsky, I.V. Maznichenko, C. Etz, A. Ernst, W. Hergert, I. Mertig, W. Wulfhekel, J. Kirschner, Phys. Rev. B 81 (2010) 195410.
[31] S.S. Parihar, H.L. Meyerheim, K. Mohseni, S. Ostanin, A. Ernst, N. Jedrecy, R. Felici, J. Kirschner, Phys. Rev. B 81 (2010) 075428.
[32] A. Picone, G. Fratesi, A. Brambilla, P. Sessi, F. Donati, S. Achilli, L. Maini, M.I. Trioni, C.S. Casari, M. Passoni, A. Li Bassi, M. Finazzi, L. Duò, F. Ciccacci, Phys. Rev. B 81 (2010) 115450.
[33] A. Picone, A. Brambilla, A. Calloni, L. Duò, M. Finazzi, F. Ciccacci, Phys. Rev. B 83 (2011) 235402.
[34] F. Donati, P. Sessi, S. Achilli, A. Li Bassi, M. Passoni, C.S. Casari, C.E. Bottani, A. Brambilla, A. Picone, M. Finazzi, L. Duò, M.I. Trioni, F. Ciccacci, Phys. Rev. B 79 (2009) 195430.
[35] G. Bussetti, M. Riva, A. Picone, A. Brambilla, L. Duò, M. Finazzi, F. Ciccacci, New J. Phys. 14 (2012) 053048.
[36] G. Bussetti, M. Riva, A. Picone, A. Brambilla, L. Duò, F. Ciccacci, M. Finazzi, Nanosci. Nanotechnol. Lett. 4 (2012) 1092.
[37] Y. Kim, C. Westphal, R. Ynzunza, Z. Wang, H. Galloway, M. Salmeron, M.V. Hove, C. Fadley, Surf. Sci. 416 (1998) 68.
[38] V. Kuznetsov, R. Kadyrov, G. Rudenskii, J. Mater. Sci. Technol. 14 (1998) 320.
[39] L. Vitos, A. Ruban, H. Skriver, J. Kollár, Surf. Sci. 411 (1998) 186.
[40] A.V. Mijiritskii, P.J.M. Smulders, V.Y. Chumanov, O.C. Rogojanu, M.A. James, D.O. Boerma, Phys. Rev. B 58 (1998) 8960.
[41] P. Luches, V. Bellini, S. Colonna, L. Di Giustino, F. Manghi, S. Valeri, F. Boscherini, Phys. Rev. Lett. 96 (2006) 106106.
[42] S. Ekelund, C. Leygraf, Surf. Sci. 40 (1973) 179.
[43] A. Calloni, A. Picone, A. Brambilla, M. Finazzi, L. Duò, F. Ciccacci, Surf. Sci. 605 (2011) 2092.
[44] D.T. Pierce, J.A. Stroscio, J. Unguris, R.J. Celotta, Phys. Rev. B 49 (1994) 14564.
[45] S. Valeri, A. Borghi, G. Gazzadi, A. di Bona, Surf. Sci. 423 (1999) 346.
[46] A. Borghi, A. di Bona, D. Bisero, S. Valeri, Appl. Surf. Sci. 150 (1999) 13.
[47] J. Goniakowski, F. Finocchi, C. Noguera, Rep. Prog. Phys. 71 (2008) 016501.
[48] C. Noguera, J. Goniakowski, Chem. Rev. 113 (2013) 4073.
[49] J. Gurgul, E. Myczak, N. Spiridis, J. Korecki, Surf. Sci. 606 (2012) 711.
[50] L. Zhang, M. Kuhn, U. Diebold, Surf. Sci. 375 (1997) 1.
[51] W.A.A. Priyantha, G.D. Waddill, Surf. Sci. 578 (2005) 149.
[52] A. Maetaki, K. Kishi, Surf. Sci. 411 (1998) 35.
[53] A. Stierle, P. Bdeker, H. Zabel, Surf. Sci. 327 (1995) 9.
[54] K. Biedermann, M. Gubo, L. Hammer, K. Heinz, J. Phys.: Condens. Matter 21 (2009) 185003.